



ELSEVIER

Coastal Engineering 38 (1999) 223–247

**COASTAL
ENGINEERING**

www.elsevier.com/locate/coastaleng

An active wave generating–absorbing boundary condition for VOF type numerical model

Peter Troch^{*}, Julien De Rouck

Department of Civil Engineering, University of Ghent, Technologiepark 9, B-9052 Zwijnaarde, Ghent, Belgium

Received 10 August 1998; received in revised form 11 August 1999; accepted 30 August 1999

Abstract

The objective of the present work is to discuss the implementation of an active wave generating–absorbing boundary condition for a numerical model based on the Volume Of Fluid (VOF) method for tracking free surfaces. First an overview of the development of VOF type models with special emphasis in the field of coastal engineering is given. A new type of numerical boundary condition for combined wave generation and absorption in the numerical model VOFbreak² is presented. The numerical boundary condition is based on an active wave absorption system that was first developed in the context of physical wave flume experiments, using a wave paddle. The method applies to regular and irregular waves. Velocities are measured at one location inside the computational domain. The reflected wave train is separated from the incident wave field in front of a structure by means of digital filtering and subsequent superposition of the measured velocity signals. The incident wave signal is corrected, so that the reflected wave is effectively absorbed at the boundary. The digital filters are derived theoretically and their practical design is discussed. The practical use of this numerical boundary condition is compared to the use of the absorption system in a physical wave flume. The effectiveness of the active wave generating–absorbing boundary condition finally is proved using analytical tests and numerical simulations with VOFbreak². © 1999 Elsevier Science B.V. All rights reserved.

Keywords: Boundary condition; Wave absorption; Numerical model; Volume Of fluid

1. Introduction

The numerical description of free surface flows including overturning wave breaking and large vertical accelerations remains a difficult task. The logical description of the

^{*} Corresponding author. Tel: +32-9264-54-89; fax: +32-9264-58-37; e-mail: peterb.troch@rug.ac.be

shape and evolution of the free surface and the formulation of accurate boundary conditions is complex. The Volume Of Fluid (VOF) technique (Hirt and Nichols, 1981) today is the most efficient and widely applicable numerical technique capable of simulating these free surface flows, and therefore is of particular importance in the field of coastal engineering. The VOF technique however is not the only existing method for treating arbitrary free surfaces. Reference is made to other methods, such as the Marker-And-Cell (MAC) method (Welch et al., 1966), the Particle Chain method (Shyy, 1994) and the Level Set method (Sethian, 1997). The VOF type models are not yet wide spread in the field of coastal engineering, but only start to develop. A very important issue is the addition of adequate wave boundary conditions in order to simulate wave propagation and reflection problems correctly. This type of boundary condition is not available in the original VOF code. A new numerical wave boundary condition based on an active wave absorption system for a physical wave flume (Frigaard and Christensen, 1994), is derived in this paper. It shows good performance with respect to absorption characteristics and only limited additional calculations are required.

The content of the paper is outlined here. First, an overview of the developments of VOF type numerical models with special emphasis on the latest developments in the field of coastal engineering is given in Section 2. Section 3 contains a description of the numerical model VOFbreak², based on the original VOF technique. In Section 4, the principle and design of the active wave generating–absorbing boundary condition that has been implemented in VOFbreak² are presented. The differences with respect to the practical use in a physical wave flume are described also. The performance and effectiveness of the numerical boundary condition is discussed in Section 5, using analytical examples and simulations with VOFbreak². Finally, Section 6 summarises the main conclusions.

2. Developments of VOF type numerical models

This section summarises the key developments of the VOF type models, and relates the progress in the field of coastal engineering. Fig. 1 shows the ‘family tree’ of VOF type models. The thick solid line connects the evolution stages of the original VOF models by the inventors of the VOF technique. The branches identify the major models developed mainly for coastal engineering applications.

The MAC method (Welch et al., 1966) was developed for the solution of viscous, incompressible and transient fluid flow problems involving free surfaces. This method used for the first time velocity and pressure directly as the dependent variables. The fluid configuration is defined using a set of marker particles moving with the fluid. These massless particles are used to determine the status of the computational cells as “full”, “empty” or “surface”, but do not influence the dynamics of the fluid flow. It was the first method to successfully treat problems involving complicated free surface motions. However, an accurate approximation of the free surface required a huge number of marker particles, and is computationally inefficient. Also, the numerical scheme was prone to instability. Several researchers subsequently improved the original MAC method.

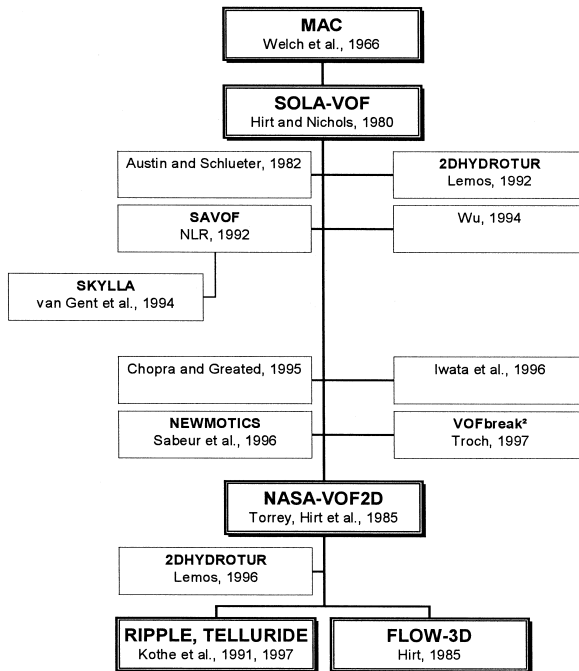


Fig. 1. Overview of key developments of VOF type numerical models with special emphasis on the progress in the field of Coastal Engineering.

The SOLA-VOF algorithm is a highly optimised variant of the MAC method, in which the free surfaces are treated by means of a single mesh-wide array. The continuity equation is satisfied using a pressure–velocity relaxation that is particularly simple to program in a staggered mesh. This method has been applied in the SOLA-VOF model (Hirt and Nichols, 1981). The main advantages are that the pressure solution does not require pressure boundary conditions, and that the SOLA-VOF model allows a more efficient tracking of the free surface. It is based on the concept of a fractional VOF for tracking free surface boundaries using the donor–acceptor approximation algorithm. The treatment of the free surface configuration using a single function F is computationally very efficient. This general-purpose code has very promising features and is generally acknowledged as the basis for all subsequent developments in the VOF-field.

Its successor code NASA-VOF2D (Torrey et al., 1985) contains several improvements. A partial-cell treatment (FAVOR) allows for curved or sloping boundaries without the need for curvi-linear co-ordinates. Fixes have been made in the donor–acceptor algorithm, and an optional conjugate gradient solver is used rather than the original successive over-relaxation method for solving the pressure equation. Both SOLA-VOF and NASA-VOF2D codes have been developed at Los Alamos National Laboratory (LANL), NM, USA.

From 1985 on, Hirt continued developments on the VOF model in the commercial CFD code FLOW-3D. It is regarded as a state-of-the-art CFD code for general

applicability. At LANL, other successor codes have been developed since then: RIPPLE (Kothe et al., 1991) for 2D and TELLURIDE (Kothe et al., 1997) for 3D simulations. In RIPPLE and TELLURIDE, a projection method is used to solve for the incompressible flow. The pressure Poisson equation is solved via a (incomplete Cholesky) conjugate gradient technique. Particularly, the modelling of surface tension problems and the modelling of the filling, cooling and solidification processes of castings have been enhanced. These models incorporate the latest advances in numerical algorithms and parallel processing.

These VOF codes have been applied in the fields of casting, coating, dynamics of drops, ship hydrodynamics, etc. In the field of coastal engineering, VOF-type models are not yet very well known or widely used. Nevertheless, during the last 5 years, there has been significant advance towards the implementation of numerical “wave flumes” using the VOF concept. This might be due partly to the increasing speed and storage memory of modern computers that become available, and partly to the rather complex structure of the numerical model.

Austin and Schluter (1982) presented the first rough application of the SOLA-VOF model in the field of coastal engineering. The model predicted the flow field in a porous armour layer of a breakwater schematised as a rectangular block system. Although in a relatively crude form, these calculations were the start of the simulation of wave propagation and interaction with structures in coastal engineering.

Lemos (1992) incorporated a $k - \varepsilon$ turbulence model in a SOLA-VOF based code 2DHYDROTUR that allowed a limited description of the turbulence field. Lemos (1992) also implemented higher order finite difference schemes in a VOF-based code for improving stability and accuracy of the numerical solutions. These improved schemes were applied to simulations of wave impact on structures, and included the computation of the wave impact forces. No wave absorption boundaries or open sea boundaries have been implemented.

The SKYLLA model (Van der Meer et al., 1992) presently being developed at Delft Hydraulics is based on SAVOF, a stripped version of SOLA-VOF obtained from the National Aerospace Laboratory (NLR) in the Netherlands. The first computations showed that it is possible to simulate breaking waves on a slope. Several extensions have been added since then. The most important are the inclusion of a conjugate gradient solver for the pressure Poisson equation (Van der Meer et al., 1992), another algorithm (FLAIR; Ashgriz and Poo, 1991) for the calculation of the F flux between adjacent cells and the subsequent free surface calculation (Petit and van den Bosch, 1992), simulation of porous flow inside permeable coastal structures, implementation of a ‘weakly reflective boundary’ (i.e., a Sommerfeld radiation boundary) (Van Gent et al., 1994). The model has been validated using both analytical and experimental data (Van Gent, 1995). The SKYLLA code is currently one of the most versatile and powerful numerical models today for applications in the field of coastal engineering.

Wu (1994) applied a VOF model based on the SOLA-VOF model for the simulation of breaking and non-breaking wave kinematics at and on vertical structures with various impermeable foreshore geometries. He simulated the complete impact pressure and the resulting loading when neglecting entrapped air. A weakly reflecting boundary condition similar to the SKYLLA model has been implemented.

Chopra and Greated (1995) used a SOLA-VOF model and included a basic model for air pocket entrapment. No further information on wave boundary conditions is provided.

Iwata et al. (1996) used a modified SOLA-VOF model for numerical comparison with experimental data from breaking and post-breaking wave deformation due to submerged impermeable structures. Waves are generated internally in the computational domain using the source generation technique (Brorsen and Larsen, 1987). Absorption of the waves is done using the Sommerfeld radiation boundary condition.

Sabeur et al. (1996) presented a modified SOLA-VOF model called NEWMOTICS. Special attention is paid to improve the free surface boundary conditions. At the wave-generating boundary, a weakly reflecting boundary condition is used. A conjugate gradient solver is implemented for use in parallel processing. More recent validation of the model is described in Waller et al. (1998). The code has been validated using theoretical and experimental data in the context of a solitary wave propagating into water of varying depth with impermeable bottom.

Troch (1997) presented the numerical model VOFbreak² based on the SOLA-VOF code. Several modifications are implemented to refine the numerical model for wave motion on and in coastal structures. Special attention is paid to applications involving rubble mound breakwaters. Wave boundary conditions are added, where any wave theory can be applied to provide the surface elevation and the velocity components in horizontal and vertical direction. The governing equations are extended, to include the simulation of porous flow inside the permeable coastal structure, by adding the Forchheimer resistance terms. The numerical model is being verified with both physical model data and prototype data. Some selected improvements from NASA-VOF2D have been implemented into VOFbreak², such as a numerical defoamer technique, and fixes on the donor–acceptor algorithm. In the next section, a more detailed description of the specific features of VOFbreak² is provided.

There is no general model presented including most of the physical processes involved, but researchers add only selected physical processes for their particular applications. It is clear that all codes still are research codes that need very careful validation before these become (coastal) engineering tools for daily use in the design process.

3. Description of the numerical model VOFbreak²

The numerical model VOFbreak², VOF-algorithm for breaking waves on breakwaters, is based on the original SOLA-VOF code (Nichols et al., 1980) capable of treating low-speed flows involving arbitrary (e.g., multiply connected) free surface configurations. The equations governing the 2D motion of an incompressible fluid in the vertical (x – z) plane are:

$$\frac{\partial u}{\partial t} + u \frac{\partial u}{\partial x} + v \frac{\partial u}{\partial z} = -\frac{1}{\rho} \frac{\partial p}{\partial x} + \nu \left(\frac{\partial^2 u}{\partial x^2} + \frac{\partial^2 u}{\partial z^2} \right) + g_x \quad (1)$$

$$\frac{\partial v}{\partial t} + u \frac{\partial v}{\partial x} + v \frac{\partial v}{\partial z} = -\frac{1}{\rho} \frac{\partial p}{\partial z} + \nu \left(\frac{\partial^2 v}{\partial x^2} + \frac{\partial^2 v}{\partial z^2} \right) + g_z \quad (2)$$

and the continuity equation:

$$\frac{\partial u}{\partial x} + \frac{\partial v}{\partial z} = 0 \quad (3)$$

where t (s) is time, u and v (m/s) are the velocity components in x and z direction res., p (N/m²) is pressure, and g_x , g_z (m/s²) are horizontal and vertical gravity components res., ρ (kg/m³) is the density of the water, ν (m²/s) is the kinematic coefficient of viscosity.

The free surface is described by introducing a function $F(x, y, t)$ that is an indicator function, whose value is one for a point inside the fluid and zero elsewhere. It is the average (integral) of F over one computational cell that represents the fraction of the cell occupied by the fluid. The VOF evolution Eq. (4) expresses that the volume fraction F moves with the fluid:

$$\frac{\partial F}{\partial t} + u \frac{\partial F}{\partial x} + v \frac{\partial F}{\partial z} = 0. \quad (4)$$

Finite difference solutions of the four unknowns u , v , p and F , are obtained on an Eulerian rectangular mesh in a Cartesian co-ordinate system (x – z):

- The Navier–Stokes Eqs. (1) and (2) are discretised using a combined FTCS/up-wind scheme. As a result, explicit approximations of the Navier–Stokes equations are used to compute the first guess for new-time-level velocities.

- To satisfy the continuity Eq. (3), i.e., to obtain a divergence-free velocity field, the pressure–velocity iteration is used. It is a variant of the Newton–Raphson relaxation technique applied to the pressure Poisson equation for incompressible flow. Using this method, pressures are iteratively adjusted in each cell and velocity changes induced by each pressure change are added to the velocities computed out of the Navier–Stokes equations.

- Finally, the VOF function F , defining the fluid regions, is updated using the donor–acceptor flux approximation for the calculation of fluxes from a donor cell to an acceptor cell. A unit value of F corresponds to a full cell, while a zero value indicates an empty cell. Cells with values between zero and one and having at least one empty neighbour cell contain a free surface. A line is constructed in each surface cell with the correct calculated surface slope and correct amount of fluid lying on the fluid size, and is used as an approximation to the actual free surface. This is a variant of a Simple Line Interface Calculation (SLIC) as used in the original Nichols–Hirt code.

A number of modifications that are specific to VOFbreak² have been introduced in the original Nichols–Hirt code. These key innovations (such as a porous flow model and wave boundary conditions) were required for simulation of wave interaction with permeable rubble mound structures, and have been summarised in Section 2 already. A more detailed description is available in Troch (1997). The VOFbreak² code is implemented using ANSI C, providing general computer compatibility, and providing a flexible code structure for adaptations with little effort. A series of post-processing tools has been developed, using Tcl/Tk for the visualisation, processing and interpretation of the computed results. Specific routines for the computation of such quantities as wave

height, run-up level, pore pressure, surface elevation, etc. can be included for easy access to calculated data.

4. An active wave generating–absorbing boundary condition

4.1. Wave boundary conditions in numerical wave flume

In Fig. 2, a conventional numerical wave flume set-up is given. Waves are generated at the left boundary of the computational domain and propagate towards a rubble mound breakwater positioned near the other boundary. The incident waves interact with the porous breakwater causing transmitted and reflected waves to propagate towards the boundaries. At the boundaries, an ‘open boundary’ or ‘absorbing boundary’ condition is required, allowing the transmitted and reflected waves to leave the computational domain without disturbing the interaction of the incident waves with the breakwater.

The numerical problem is similar to the wave absorption problems in a physical wave flume. Therefore in principle, the same solutions could be applied in the numerical flume. Schäffer and Klopman (1997) give an overview of the basic concepts of wave absorption in physical wave flumes.

However, in order to increase the computational efficiency of the calculations, a number of constraints are present. These are very important in the final choice of the numerical wave boundary conditions. A very important constraint is that the length of the numerical wave flume should be as short as possible for reasonable CPU time. Therefore, the numerical wave flume requires a relatively short foreshore (one or two wavelengths), and a very short lee-side (maximum one wavelength). The wave absorption techniques need to perform in these conditions. Also an efficient and simple numerical technique for wave absorption might be more favourable than the simulation of, e.g., a conventional progressive wave absorber requiring considerable length and mesh size.

The generation of incident waves is implemented in VOFbreak² using boundary generation. Any wave theory can be used to provide the surface elevation $\eta(x_0, t)$ and the velocity components $u(x_0, z, t)$ and $v(x_0, z, t)$ at the left boundary ($x_0 = 0$). For the simulations in this paper, linear wave theory is used. Another efficient wave generation technique is source generation (Brorsen and Larsen, 1987) where the volume

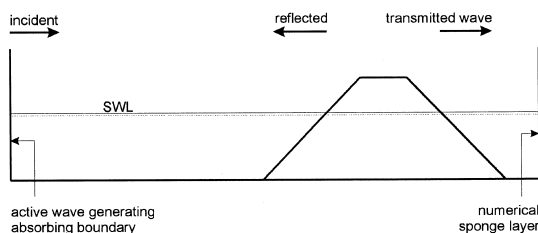


Fig. 2. Conventional numerical wave flume set-up with numerical boundary conditions for the study of wave interaction with porous rubble mound breakwater.

from the incident wave is added inside the computational domain. The advantage of this latter method is that the generation of the incident waves is not disturbed by the reflected waves. The disadvantage is that the length of the computational domain is considerably increased because a relatively long absorption layer is required for absorption of the reflected waves at the boundaries. Iwata et al. (1996) has successfully implemented the source generation technique in a SOLA-VOF model. The absorption layer required up to six wavelengths for sufficient wave absorption.

The wave absorption generally is divided into active systems and passive systems. An active system provides an active response to the waves; a passive system damps (mostly by energy dissipation) the wave motion. For this application, the transmitted waves are passively absorbed using an efficient numerical sponge layer technique from Larsen and Dancy (1983). A detailed discussion of the numerical sponge layer performance in the VOFbreak² model is described in Troch and De Rouck (1998). The reflected waves are actively absorbed at the wave-generating boundary using an active wave absorption technique. The active wave generating–absorbing system is discussed in more detail in the next section.

4.2. Principle

The active wave generating–absorbing system implemented in the numerical wave flume is based on the AWASYS system (Frigaard and Christensen, 1994) from Aalborg University. The AWASYS system originally is based on the simultaneous on-line measurement of the surface elevation at two different points, by means of conventional wave height meters. The system for VOFbreak² is based on a velocity meter based system because velocities are readily (or computationally cheap) available from the computations. Hald and Frigaard (1996) show that the performance (i.e., the absorption characteristics) of both elevations and velocities systems is similar.

Fig. 3 shows the wave flume set-up with the wave generating–absorbing boundary at location $x_0 = 0$ and the co-located velocity meters (u , v) at location (x_1, z_1) . The water depth in the flume is d (m). The principle of the active wave generating–absorbing system requires two steps. First, an on-line detection of the reflected wave field is performed using the set of spatially co-located velocities (u , v). Secondly, the wave generator has to generate the incident wave and an additional wave, which cancels out

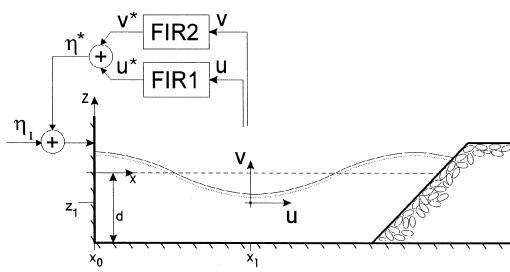


Fig. 3. Definition sketch of the numerical wave flume set-up and the principle of the active wave generating–absorbing boundary condition.

the reflected wave propagating towards the boundary. Fig. 3 shows schematically the principle of the system. The correction signal η^* that cancels out the reflected wave, is determined from superposition of the two filtered velocity signals $u^* + v^*$. The digital Finite Impulse Response (FIR) filters are operated using a time-domain discrete convolution of the velocities (u , v) and the impulse response h^i , where $i = u$ or v ; e.g., for the u velocity component:

$$u^*[n] = \sum_{j=0}^{J-1} h^u[j]u[n-j] \quad (5)$$

where J is the number of filter coefficients, and $u^*[n] = u^*(n\Delta t_f)$ is the filter output at time $t = n\Delta t_f$, where Δt_f is the filter time interval.

Having outlined the principle of the active wave generation–absorption, the only task remaining is the design of the corresponding frequency response function $H(f)$ of the filters from which the impulse response function $h(t)$ is easily derived using inverse Fourier transform.

4.3. Frequency response of digital filter

The complex frequency response $H^i(f)$ for each filter is composed of a gain $C^i(f)$ and a phase $\varphi^i(f)$, where $i = u$ or v :

$$\text{Re}.H^i(f) = C^i(f)\cos(\varphi^i(f)) \quad (6)$$

$$\text{Im}.H^i(f) = C^i(f)\sin(\varphi^i(f)).$$

The derivation of the gain $C^i(f)$ and the phase $\varphi^i(f)$ is given in this section.

The derivation of the frequency response is limited here to only one regular wave component with wave frequency f (wave period $T = 1/f$). The method is easily extendable for irregular waves. Using linear wave theory, the horizontal and vertical velocity components $u(x_1, z_1, t)$ and $v(x_1, z_1, t)$ at location (x_1, z_1) are composed of an incident and a reflected part:

$$u(x_1, z_1, t) = u_I(x_1, z_1, t) + u_R(x_1, z_1, t) \quad (7)$$

$$v(x_1, z_1, t) = v_I(x_1, z_1, t) + v_R(x_1, z_1, t)$$

where:

$$u_I(x_1, z_1, t) = a_I \omega \frac{\cosh k(d + z_1)}{\sinh kd} \cos(\omega t - kx_1 + \varphi_I) \quad (8)$$

$$u_R(x_1, z_1, t) = -a_R \omega \frac{\cosh k(d + z_1)}{\sinh kd} \cos(\omega t + kx_1 + \varphi_R)$$

$$v_I(x_1, z_1, t) = -a_I \omega \frac{\sinh k(d + z_1)}{\sinh kd} \sin(\omega t - kx_1 + \varphi_I)$$

$$v_R(x_1, z_1, t) = -a_R \omega \frac{\sinh k(d + z_1)}{\sinh kd} \sin(\omega t + kx_1 + \varphi_R)$$

where $a = a(f)$ is wave amplitude, $k = k(f)$ is wave number, $\omega = 2\pi f$ is angular frequency, $\varphi = \varphi(f)$ is phase angle. The indices I en R denote incident and reflected, respectively.

At the left boundary $x_0 = 0$, the surface elevation $\eta(x_0, t)$ of the wave component is composed of the incident and the reflected surface elevations:

$$\eta(x_0, t) = \eta_I(x_0, t) + \eta_R(x_0, t) \quad (9)$$

from where:

$$\eta(x_0, t) = a_I \cos(\omega t - kx_0 + \varphi_I) + a_R \cos(\omega t + kx_0 + \varphi_R). \quad (10)$$

The wave component $\eta_{-R}(x_0, t)$ that has to be generated at the left boundary in order to cancel out the reflected component $\eta_R(x_0, t)$, has the same amplitude as, and is in opposite phase with $\eta_R(x_0, t)$:

$$\eta_{-R}(x_0, t) = a_R \cos(\omega t - kx_0 + \varphi_R + \pi). \quad (11)$$

The application of a filter operator on the horizontal velocity $u(x_1, z_1, t)$ results in a modified signal $u^*(x_1, z_1, t)$ with gain C^u and phase shift φ^u (Christensen, 1995):

$$u^*(x_1, z_1, t) = u_I^*(x_1, z_1, t) + u_R^*(x_1, z_1, t) \quad (12)$$

$$\begin{aligned} u^*(x_1, z_1, t) = & C^u a_I \omega \frac{\cosh k(d + z_1)}{\sinh kd} \cos(\omega t - kx_1 + \varphi_I + \varphi^u) \\ & - C^u a_R \omega \frac{\cosh k(d + z_1)}{\sinh kd} \cos(\omega t + kx_1 + \varphi_R + \varphi^u). \end{aligned} \quad (13)$$

Similarly for the application of a filter operator on the vertical velocity $v(x_1, z_1, t)$:

$$v^*(x_1, z_1, t) = v_I^*(x_1, z_1, t) + v_R^*(x_1, z_1, t) \quad (14)$$

$$\begin{aligned} v^*(x_1, z_1, t) = & -C^v a_I \omega \frac{\sinh k(d + z_1)}{\sinh kd} \sin(\omega t - kx_1 + \varphi_I + \varphi^v) \\ & - C^v a_R \omega \frac{\sinh k(d + z_1)}{\sinh kd} \sin(\omega t + kx_1 + \varphi_R + \varphi^v). \end{aligned} \quad (15)$$

Assuming

$$\varphi^u = \varphi^v - \pi/2; \quad (16)$$

and superposition of the filtered velocities yields the correction signal η^* :

$$\eta^*(x_0, t) = u^*(x_1, z_1, t) + v^*(x_1, z_1, t) \quad (17)$$

$$\begin{aligned} \eta^*(x_0, t) = & a_I \omega \left(C^u \frac{\cosh k(d + z_1)}{\sinh kd} - C^v \frac{\sinh k(d + z_1)}{\sinh kd} \right) \\ & \times \cos(\omega t - kx_1 + \varphi_I + \varphi^u) - a_R \omega \left(C^u \frac{\cosh k(d + z_1)}{\sinh kd} \right. \\ & \left. + C^v \frac{\sinh k(d + z_1)}{\sinh kd} \right) \cos(\omega t + kx_1 + \varphi_R + \varphi^u). \end{aligned} \quad (18)$$

Expressing that the superposition of the filtered velocity signals $\eta^* = u^* + v^*$ at position (x_1, z_1) is equal to the wave component $\eta_{-R}(x_0, t)$ that absorbs the outgoing reflected wave at the boundary ($x_0 = 0$) yields the expressions for the theoretical gain and theoretical phase for both filters:

$$\eta^*(x_0, t) = \eta_{-R}(x_0, t) \quad (19)$$

$$C^u(f) = -\frac{1}{2\omega} \frac{\sinh kd}{\cosh k(d + z_1)} \quad (20)$$

$$\varphi^u(f) = -kx_1 + \pi \quad (21)$$

$$C^v(f) = -\frac{1}{2\omega} \frac{\sinh kd}{\sinh k(d + z_1)} \quad (22)$$

$$\varphi^v(f) = -kx_1 + \pi + \pi/2. \quad (23)$$

4.4. Design of digital filters

The practical design of both filters in the specified frequency range is accomplished following the guidelines given in Frigaard and Brorsen (1995) and Christensen (1995). The theoretical and realised frequency responses of each filter are compared visually to the frequency response obtained by a forward Fourier transform of the filter coefficients $h[j]$. For high frequencies (e.g., $f > 2$ Hz), zero gain is prescribed to avoid quick transitions in the phase shift. To avoid the singularity in the gain at $f = 0$ Hz, a second order polynomial is fitted to the theoretical gain. A tapering of the filter coefficients is applied to get a more stable digital filter. The frequency resolution of the filter, Δf_f , in the frequency response is found from $\Delta f_f = 1/(J\Delta t_f)$, the sample frequency is $f_{sf} = 1/\Delta t_f$ and the filter duration is $T_0 = J\Delta t_f$.

Fig. 4 shows an example of the practical realisation of the impulse response $h^i(t)$ from the gain $C^i(f)$ and phase $\varphi^i(f)$ of the two filters, where $i = u$ or v . The geometry that has been used for this realisation of filters has a water depth $d = 0.20$ m, and the location of co-located velocity measurements is at $x_1 = 2.99$ m, $z_1 = -0.05$ m. The following filter characteristics have been chosen: number of filter coefficients $J = 100$ and filter duration $T_0 = 10.0$ s (with cut-off frequencies $f_{LOW} = 0.40$ Hz and $f_{HIGH} = 1.25$ Hz), from where filter time interval $\Delta t_f = 0.10$ s, frequency resolution $\Delta f_f = 0.10$ Hz and filter sample frequency $f_{sf} = 10.0$ Hz. These filters have been used in the numerical examples in Section 5.

4.5. Differences with respect to the use in physical wave flume

In this section, the differences with respect to the design of the wave absorption system in a physical wave flume are discussed in more detail.

The velocity-based filters are easier to realise than the elevation based filters because there is only one singularity present in the gain $C^i(f)$ at $f = 0$ Hz. This means that the

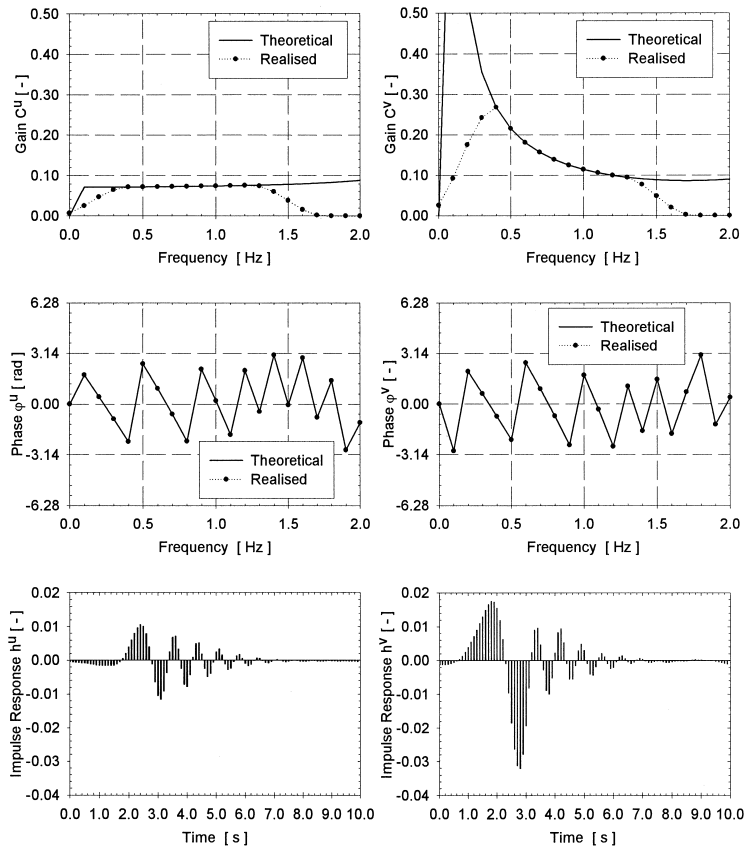


Fig. 4. Theoretical and realised gain and phase of the filters with corresponding impulse response functions. $J = 100$, $T_0 = 10.0$ s, $x_1 = 2.99$ m, $z_1 = -0.05$ m, $d = 0.20$ m, from where $\Delta t_f = 0.10$ s, $\Delta f_f = 0.10$ Hz, $f_{st} = 10.0$ Hz.

gain curve slope is not so steep and that less filter coefficients J are required to describe the gain information.

At the end of each simulation time step, the velocities and pressures are available for further use without any additional computation. These are the direct unknowns solved from the Navier–Stokes Eqs. (1)–(3). The use of free surface elevation information in the wave absorption system requires additional expensive calculation time. The determination of the free surface in each cell is an iterative calculation algorithm based on the F function information, and the free surface generally is not required at each time step of the simulation.

The AWASYS system in a physical wave flume set-up requires real-time response of the wave paddle to the reflected waves. Therefore, the filter convolution has to be carried out in real-time and only a limited number of filter coefficients J are allowable. In the system used for the numerical wave flume, no real-time response is necessary. There is sufficient time available between consecutive time steps: basically the code

waits for the calculation of the convolutions before proceeding with the calculations. Therefore, longer filters are applicable improving the efficiency of the numerical boundary condition.

The filter coefficients $h[j]$, are defined at J discrete frequency intervals. In between the frequency intervals, the obtained filter characteristics might deviate from the theoretical gain and phase. If the generated wave components are defined at the same frequency intervals as the filter coefficients this causes no problems. The design of the filters becomes straightforward and is simpler than in a physical wave flume.

Execution of the filter convolution is required only at regular time steps Δt_f . Usually, the time step Δt_{VOF} of the numerical simulation is smaller than the time step of the convolution Δt_f . This means that not at all time steps of the simulation a corrected elevation η^* will be available to add to the incident wave elevation η_i . An extrapolation using previous time step values of η^* may be applied. For these tests, simply the previous corrected elevation is used until a new value becomes available. This causes the input wave signal to look slightly like a step signal. Typically for the simulations in this paper, the simulation time step is five times smaller than the filter time step: $\Delta t_f = 5\Delta t_{\text{VOF}}$. The associated error is considered being negligible.

4.6. Comparison with weakly reflecting boundary condition

Another wave boundary treatment, commonly referred to as the “weakly reflecting boundary condition”, is used for combined wave generation and absorption in VOF type numerical models. It has been used first in the SKYLLA code (Petit and van den Bosch, 1992), and in other codes subsequently (see Section 2 for a review). Assuming a non-dispersive linear wave component, the surface elevation and velocities of incident and reflected wave satisfy a set of hyperbolic equations, including the wave celerity c , e.g., for the surface elevation η :

$$\frac{\partial \eta}{\partial t} - c \frac{\partial \eta}{\partial x} = \frac{\partial \eta_i}{\partial t} - c \frac{\partial \eta_i}{\partial x} \quad (24)$$

where the subscript i refers to the incident wave. Thus, knowing the form and celerity of the wave leaving the computational domain, a modification can be calculated for elevation and velocities allowing the reflected wave to leave the domain during wave generation.

The hyperbolic Eq. (24) allows only regular waves with one celerity c to leave the computational domain. In the case of irregular waves with various celerities, Petit and van den Bosch (1992) suggest to choose a suitable value of the celerity c (e.g., the value of c associated with the peak period), or to use a higher order weakly reflecting boundary condition describing all waves with different celerities c_j , $j = 1 \dots N$, travelling out of the computational domain:

$$\prod_j \left(\frac{\partial}{\partial t} - c_j \frac{\partial}{\partial x} \right) \eta = \prod_j \left(\frac{\partial}{\partial t} - c_j \frac{\partial}{\partial x} \right) \eta_i. \quad (25)$$

The use of the weakly reflecting boundary condition (24) has been proved to be efficient for regular waves for both wave generation–absorption and absorption only

modes (Van Gent, 1995). Minor modifications to Eq. (24) were required to account for a stretched velocity profile (i.e., the prescription of the velocities near the corrected free surface where the incident wave generation procedure does not provide velocities), and the subsequent correction for conservation of momentum. The application of Eq. (25) has not yet been presented and appears tedious to implement in a code. Only a limited number of values c_j are acceptable for the effective use of this type of boundary condition.

There is no major advantage in choosing one boundary treatment or the other for regular waves. However for the application of irregular waves, the active wave generating–absorbing boundary condition intrinsically has the capability to treat irregular waves in the same way as regular waves. The performance of this boundary condition is only achieved by the design of the filters. It is also possible to derive non-linear digital filters if this would be required for particular applications.

5. Performance of the numerical wave boundary condition using numerical examples

Two types of numerical examples are given that show the performance of the wave generating–absorbing boundary condition. First, a set of analytical examples with known incident and reflected waves is described. Secondly, a number of numerical simulations using the boundary condition in VOFbreak² are given.

5.1. Analytical example

In order to evaluate the absorption method, we will look at an analytical example with known incident and reflected wave components. The error is defined by the difference between the filtered correction signal $\eta^*(x_0, t)$ and the wave component $\eta_{-R}(x_0 = 0, t)$ at the boundary. The error is zero when the calculated signal η^* is identical to the actual signal η_{-R} .

The geometry and the filters are taken from Section 4.4 (and Fig. 4), and are used for all examples in this and the following section. The velocities at location (x_1, z_1) are described by Eq. (7) using incident and reflected components given by Eq. (8), corresponding to 50% reflection, and read here:

$$u(x_1, z_1, t) = \sum_i \left[0.01 \cdot 2\pi f_i \frac{\cosh k_i(d + z_1)}{\sinh k_i d} \cos(2\pi f_i t - k_i x_1) - 0.50 \cdot 0.01 \cdot 2\pi f_i \frac{\cosh k_i(d + z_1)}{\sinh k_i d} \cos(2\pi f_i t + k_i x_1) \right] \quad (26)$$

$$v(x_1, z_1, t) = \sum_i \left[-0.01 \cdot 2\pi f_i \frac{\sinh k_i(d + z_1)}{\sinh k_i d} \sin(2\pi f_i t - k_i x_1) - 0.50 \cdot 0.01 \cdot 2\pi f_i \frac{\sinh k_i(d + z_1)}{\sinh k_i d} \sin(2\pi f_i t + k_i x_1) \right]. \quad (27)$$

Table 1

Characteristics of wave components for each test case of the analytical example

Test no.	Subscript i	n_i [–]	f_i [Hz]	T_i [s]	k_i [m ^{−1}]
1	1	5	0.50	2.00	2.32
2	1	5	0.50	2.00	2.32
	2	8	0.80	1.25	3.93
	3	10	1.00	1.00	5.18
3	1	5.5	0.55	1.82	2.57
4	1	5.5	0.55	1.82	2.57
	2	8.5	0.85	1.18	4.24
	3	10.5	1.05	0.95	5.55

The wave component η_{-R} is defined using Eq. (11) and reads here:

$$\eta_{-R}(x_0, t) = \sum_i [0.50 \cdot 0.01 \cos(2\pi f_i t - kx_0 + \pi)]. \quad (28)$$

The subscript i in these Eqs. (26)–(28) refers to the number of wave components that have been used in the tests, according to Table 1. Test no. 1 includes one regular wave component and test no. 2 includes three components constituting an irregular wave

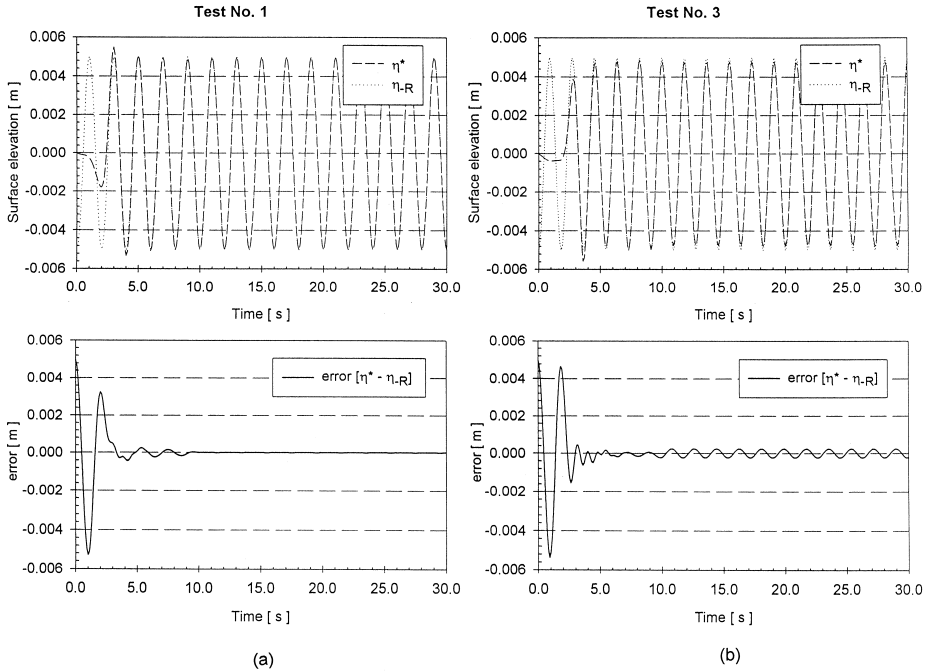


Fig. 5. Comparison between the surface elevations η^* and η_{-R} with associated error for regular waves, with (a) $f_1 = 5\Delta f$, and (b) $f_1 = 5.5\Delta f$.

signal. This allows showing the genuine use of the method for irregular waves. The velocity and absorption signals, Eqs. (26)–(28), respectively, are sampled with a sample frequency of 10.0 Hz.

Fig. 5a and Fig. 6a illustrate the performance of the absorption method when the frequencies f_i of the wave components are all coinciding with some discrete frequencies of the filters, i.e., $f_i = n_i \Delta f_f$, where $\Delta f_f = 0.10$ Hz. For both tests no. 1 (regular wave) and no. 2 (irregular wave), the error is zero, so the method is exact, as expected for signals consisting of energy only placed at these discrete frequencies. It is also seen that during the ‘warm up’ time T_0 of the filters errors are present.

Test nos. 3 and 4 are identical to test nos. 1 and 2, respectively, except that the wave frequencies f_i are not coinciding with the discrete filter frequencies, but are placed midway between the frequencies. This represents the worst case situation. Fig. 5b and Fig. 6b show that errors are present after warm up. One way to improve the result is to taper the filter coefficients (Frigaard and Brorsen, 1995). The tapering generates a more stable output of the digital filter. Fig. 7 shows the errors associated with the tapered filters used for test nos. 3 and 4, in comparison to the errors obtained without tapering (taken from Fig. 5b and Fig. 6b, respectively). The errors are shown after warming up of the filters for $t = 10.0$ s till $t = 30.0$ s. Another way to improve the performance of the filters is to use more filter coefficients (e.g., $J = 200$), and consequently the resolution of the filter increases ($\Delta t_f = 0.05$ s for $T_{0,f} = 10.0$ s). Fig. 7 also shows the errors using tapered filters with double resolution.

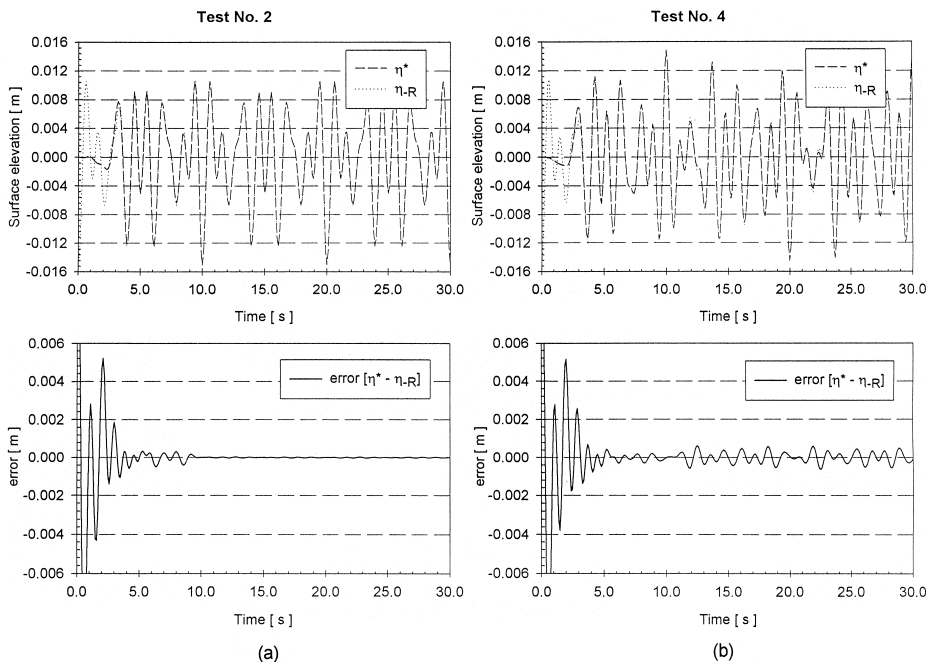


Fig. 6. Comparison between the surface elevations η^* and η_{-R} with associated error for irregular waves, with (a) $f_1 = 5\Delta f$, $f_2 = 8\Delta f$, $f_3 = 10\Delta f$ and (b) $f_1 = 5.5\Delta f$, $f_2 = 8.5\Delta f$, $f_3 = 10.5\Delta f$.

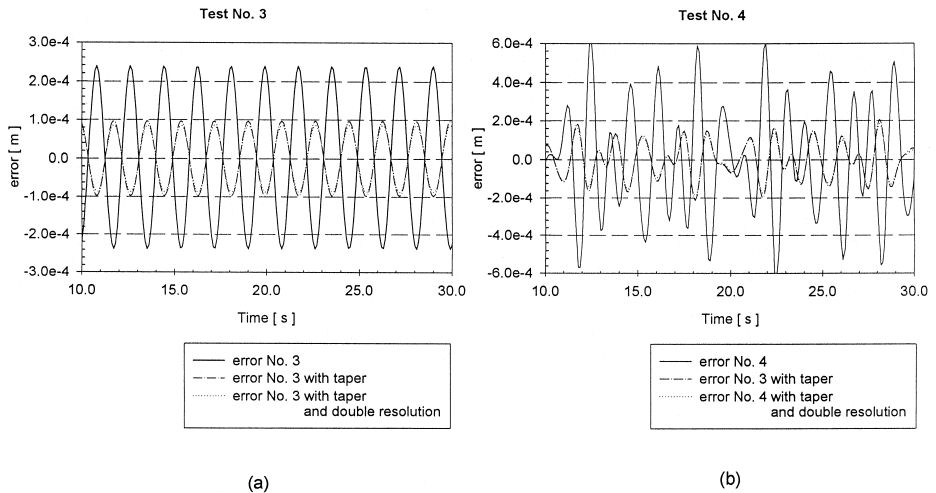


Fig. 7. Comparison between errors for (a) regular waves, and (b) irregular waves, with $f_1 = 5.5\Delta f$, $f_2 = 8.5\Delta f$, $f_3 = 10.5\Delta f$, for the case of original filters, the case of cosine tapered filters and the case of cosine tapered filters with double resolution.

Table 2 summarises the errors associated with the tests from the analytical example. The error is expressed as the variance of the error signals, calculated from $t = 10.0$ s till $t = 30.0$ s.

From Table 2, it is seen that the errors in test nos. 1 and 2 are negligible. This proves that the method is exact for both regular and irregular waves, as discussed before. The errors involved in test nos. 3 and 4 reduce considerably by tapering the filters. The use of filters with double resolution additionally decreases the error. However, the effect of this latter manipulation is very small and may seem negligible compared to the additional computational effort involved in the calculation of the convolution sums of the filters.

For practical use of the absorption method in a numerical model, therefore, generation of waves should not start before the filters are warmed up in order to reduce initial

Table 2
Variance of errors associated with each test case of the analytical example

Test no.	Variance of error ($\times 10^{-9}$) [m ²]
1	0.01
2	0.21
3	28.45
4	84.26
3 with taper	4.77
4 with taper	8.58
3 with taper and double resolution	3.71
4 with taper and double resolution	6.73

errors in the wave generation–absorption process. Also the wave components of the generated incident wave field should match the discrete filter frequencies for better performance.

5.2. Numerical simulation using VOFbreak²

To illustrate the effectiveness of the active wave generating–absorbing boundary condition for a VOF type numerical model, a number of numerical simulations have been carried out using VOFbreak². Both the cases of pure absorption and simultaneous generation and absorption of waves are treated.

Note that for the numerical simulations no so-called “Stokes drift” (i.e., asymmetry of free surface velocities over one wave period indicating that more fluid moves in the wave direction under the crest than under the trough) compensation has been included at the wave boundary. For applications including longer time series, this compensation has to be considered as the importance increases. Otherwise, mass would be accumulated inside the computational domain.

The corrected surface elevation η^* at the boundary is obtained by digital filtering of the two velocity signals, and added to the surface elevation η_i of the incident wave. The velocity components of the velocity profile at the boundary are obtained from this corrected surface elevation $\eta_i + \eta^*$ using linear wave theory. The horizontal velocity component at each vertical boundary cell face is proportional to the corrected surface elevation. The vertical velocity component at each horizontal boundary cell face is obtained by digital filtering of the corrected surface elevation signal.

5.2.1. Absorption of incident waves

For the case of pure absorption, consider a computational domain with a wave generating boundary at the right boundary, $x_R = 5.42$ m (Fig. 8). At the left boundary, $x_0 = 0.0$ m, waves are absorbed using the wave generating–absorbing boundary condition. From a cold start, waves are generated at the x_R boundary and propagate towards the x_0 boundary in water depth $d = 0.20$ m. The incident waves have a range of wave heights and have one wave period $T = 2.0$ s, from where $x_R = 2L$, where L is the wavelength obtained from linear theory. The incident waves are tapered with a hyperbolic tangent function during the first wave period to suppress transients due to shocks. Wave generation is stopped at $t = 60$ s. The wave generating–absorbing boundary x_0 will operate in absorption mode only and will consequently generate the wave component η_{-R} that absorbs the incident wave. This absorbing wave component η_{-R} is

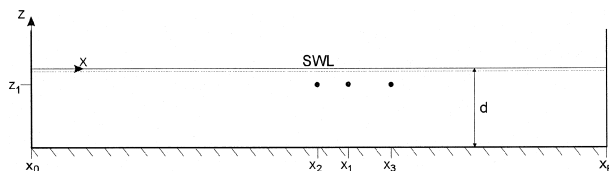


Fig. 8. Definition sketch of the computational domain used for the numerical simulations in VOFbreak². Waterdepth is $d = 0.20$ m, $x_0 = 0.0$ m, $x_1 = 2.99$ m, $x_2 = 2.71$ m, $x_3 = 3.39$ m, $x_R = 5.42$ m, $z_1 = -0.05$ m.

calculated from the superposition of the filtered velocity signals at $x_1 = 2.99$ m, $z_1 = -0.05$ m. The performance is proved by comparing the generated elevation η_{-R} and corresponding velocities at the absorbing x_0 boundary with the elevations and velocities, respectively, at the generating x_R boundary. The velocity components are taken at the level $z_1 = -0.05$ m. Optimal performance is achieved when the incident waves are absorbed completely at x_0 , i.e., when elevation and velocities at x_0 are equal to elevation and velocities at x_R .

The numerical parameters are: grid dimensions $\Delta x = \Delta y = 0.02$ m, kinematic viscosity $\nu = 1.3 \times 10^{-4}$ m²/s, upwind factor $\alpha = 0.30$, time step $\Delta t_{\text{VOF}} = 0.01$ s. Four tests are carried out (see Table 3) using four different wave heights: in the first test, regular waves with a small wave height $H_i = 0.001$ m are used as approximation to linear waves. In the other three tests, the wave height of the regular waves is increased.

Fig. 9 shows a typical result from the numerical simulations (taken from test no. Abs2). The time series of the surface elevation η and velocities (u , v) at the wave generating boundary x_R and at the wave absorbing boundary x_0 are shown. From Fig. 9, it is seen that the absorption of the waves starts only after two wave periods when the incident wave has reached the other boundary. The wave absorbing component η_{x_R} is in opposite phase with the incident wave component, as expected. The error ε_{abs} is quantified as the normalised difference of the wave height of the incident and absorbed wave trains, or:

$$\varepsilon_{\text{abs}} = \frac{|H_i - H_{\text{abs}}|}{H_i}, \quad (29)$$

where H_i is the wave height of the incident wave at the x_R boundary, and H_{abs} is the wave height of the computed absorbed wave at the x_0 boundary. As soon as the wave generation has stopped at $t = 60$ s, the wave absorbing boundary absorbs the last two waves propagating inside the flume, and very soon afterwards the water inside the flume returns quiescent.

Both velocity components u and v behave in the same way as the elevations. Now velocities are in phase, as expected. At the beginning of the wave absorption process, a small phase difference is present however in the vertical velocity component and disappears after five wave periods.

Table 3 summarises the errors for all test cases of the numerical simulation. H_{abs} is derived from spectral analysis on the elevation time series η_{x_0} . In test no. Abs1, the error

Table 3

Wave heights and error associated with each test case of the numerical simulation in absorption mode only, using VOFbreak²

Test no.	$H_i = H_{x_R}$ [m]	H_i / d [–]	$H_{\text{abs}} = H_{x_0}$ [m]	ε_{abs} [–]
Abs1	0.001	1/200	0.001	0.0
Abs2	0.01	1/20	0.009	0.08
Abs3	0.02	1/10	0.018	0.10
Abs4	0.03	1/6.7	0.026	0.13

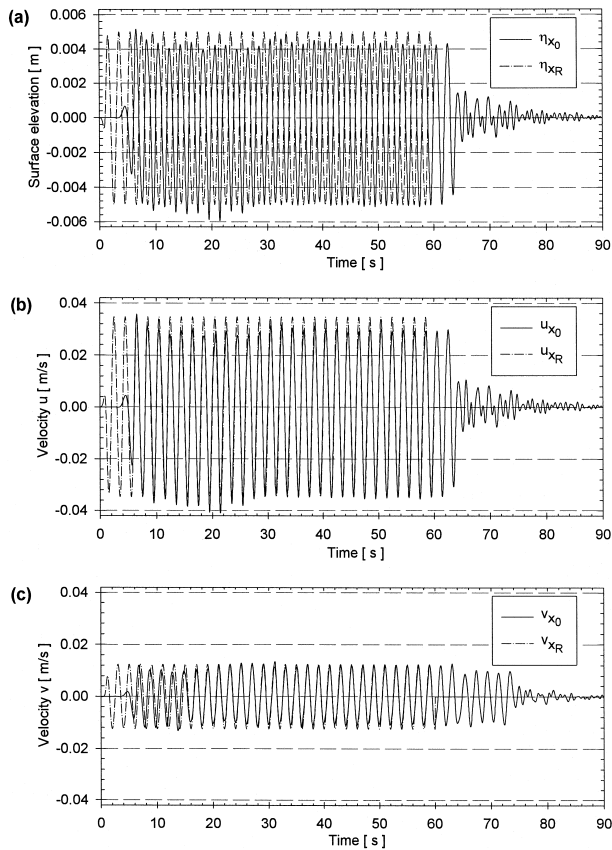


Fig. 9. Time series at $x_0 = 0.0$ m and at $x_R = 5.42$ m for: (a) surface elevation η , (b) horizontal velocity component u , (c) vertical velocity component v . Test case no. Abs2 with incident wave characteristics $H_i = 0.01$ m, $T = 2.0$ s, $d = 0.20$ m. Velocity components at level $z_1 = -0.05$ m.

ε_{abs} is equal to zero: the wave absorbing boundary condition performs excellent for a linear wave. The error increases as the wave height becomes larger and waves become more non-linear. This indicates that there is some reflection from the wave absorbing boundary back into the computational domain. However, the amount of reflection in general is less than 15% indicating that reflection is of minor importance.

5.2.2. Generation and absorption of waves

For the case of simultaneously generating and absorbing waves at the wave generating-absorbing boundary x_0 , a standing wave is generated in the computational domain (Fig. 8). The incident wave has a wave height $H_i = 0.01$ m, wave period $T = 2.0$ s in water depth $d = 0.20$ m. The right boundary x_R now is considered to be an impermeable vertical wall with 100% reflection. Fig. 10 shows time series at antinode $x_2 = 4/4L = 2.71$ m and at node $x_3 = 5/4L = 3.39$ m for the horizontal and vertical

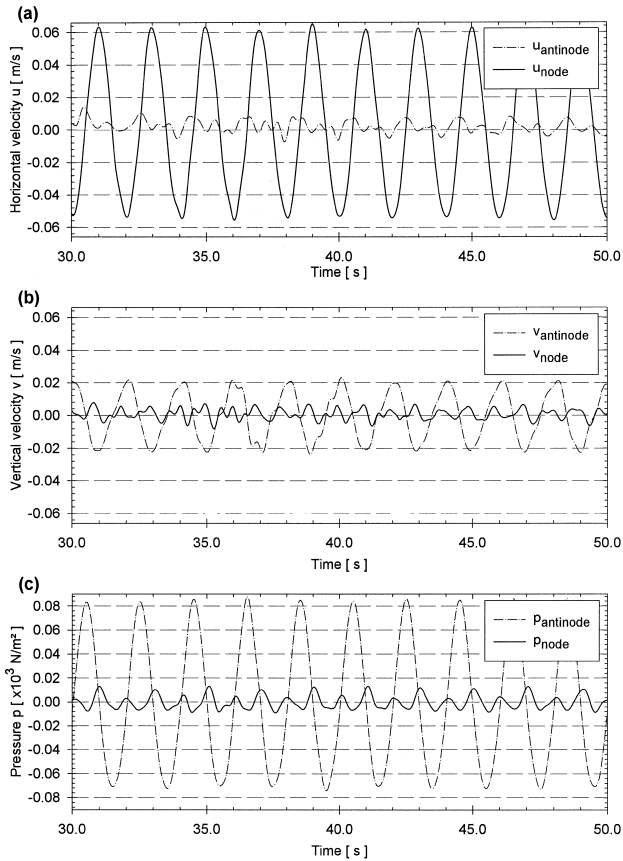


Fig. 10. Time series at antinode $x_2 = 2.71$ m and at node $x_3 = 3.39$ m for: (a) horizontal velocity component u , (b) vertical velocity component v , (c) dynamic pressure p . Incident wave characteristics $H_i = 0.01$ m, $T = 2.0$ s, $d = 0.20$ m. Velocity components and pressure at level $z_1 = -0.05$ m.

velocity components (u , v) and for the pressure p at level $z_1 = -0.05$ m from the numerical simulation. For a perfect standing wave pattern, the dynamic pressure p and the vertical velocity component v should equal zero at the node whereas the horizontal velocity component u should have maximum amplitude, and vice versa at the antinode. The error is indicated by the deviation of velocities and pressure from the expected zero value. From Fig. 10, it is seen that there is good agreement between the theoretical standing wave pattern and the obtained results at the node and antinode. The error will decrease for smaller wave heights and increase for larger wave heights according to the results from Table 3. Fig. 11 illustrates the simulated standing wave pattern by showing snapshots of the free surface configuration and velocity field at five time instants within a time interval of 2.0 s.

Finally, Fig. 12 shows the time series of the surface elevation at the wave generating–absorbing boundary x_0 for a typical example application where a reflecting

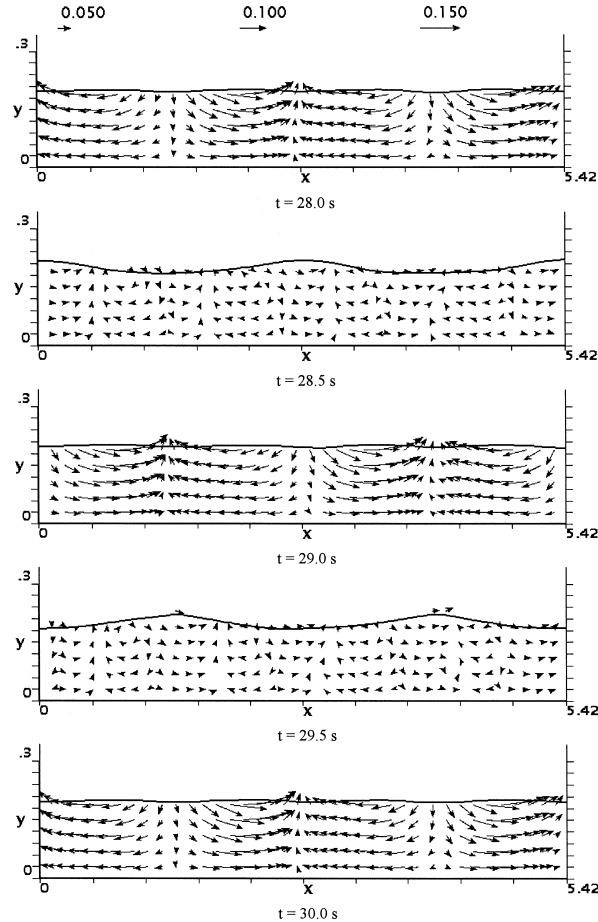


Fig. 11. Snapshots of free surface configuration and velocity field for standing wave during one wave period. Incident wave characteristics $H_i = 0.01$ m, $T = 2.0$ s, $d = 0.20$ m.

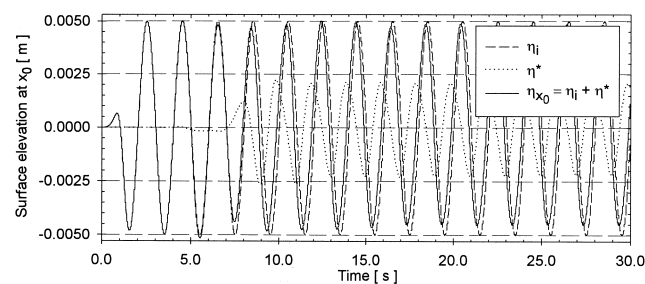


Fig. 12. Time series of surface elevations at the wave generating–absorbing boundary x_0 , where η_i is the surface elevation of the incident wave component, η^* is the correction signal absorbing the reflected wave component, and $\eta_i + \eta^*$ is the actual generated surface elevation at the boundary. Incident wave characteristics: $H = 0.01$ m, $T = 2.0$; $d = 0.20$ m.

structure is positioned near the right wall. The reflection coefficient of the structure is 45%. The generated regular wave has a wave height $H_i = 0.01$ m and wave period $T = 2.0$ s in water depth $d = 0.20$ m. The solid line shows the actual generated surface elevation η_{x_0} at the boundary, i.e., the superposition of the incident regular wave and the corrected wave: $\eta_i + \eta^*$. The dotted line is the correction signal η^* and shows how the reflected wave is building up and reaches a steady state behaviour. Finally, when subtracting the corrected signal η^* from the actual signal $\eta_i + \eta^*$, the original regular incident wave signal can be retrieved. From Fig. 12, it is also seen that the reflected component has a wave height very close to 45% of the incident wave height. This last example also illustrates the stable behaviour of the active wave generating–absorption system.

6. Conclusions

An overview of the history of development of VOF type numerical models has been presented. Special attention has been paid to the progress made in the field of coastal engineering. Most of the models here are based on the older SOLA-VOF code. At present, no general engineering tool based on a VOF model is available for design purposes. The specific features of the VOFbreak² code have been presented in more detail.

A numerical boundary condition for combined wave generation and absorption has been presented. The boundary condition has been implemented for the first time in a numerical wave flume based on the VOF model. As the horizontal and vertical velocity components are solved directly from this VOF model, an active wave absorption system based on the velocities is a very efficient and effective boundary condition. The theoretical derivation and practical design of the digital filters used in the active wave generating–absorbing boundary condition have been discussed. Compared to the performance of the system in physical wave flumes the numerical boundary condition has numerous specific properties, which increase significantly the performance of the active wave absorption system in a numerical model. The effectiveness of the new wave boundary condition has been proved by using analytical tests and by using simulations with the numerical model VOFbreak².

Acknowledgements

The development of this work originated during the EC MAST 2 project MAS02-CT92-0023, and continues during the EC MAST 3 project OPTICREST MAS3-CT97-0116. The financial support of EC is greatly acknowledged. Discussions with Ass. Prof. Michael Brorsen and especially with Ass. Prof. Peter Frigaard, the designer of the AWASYS system, both from Aalborg University, Denmark, on wave boundary modelling are very much appreciated.

References

- Ashgriz, N., Poo, J.Y., 1991. FLAIR: Flux Line-Segment Model for Advection and Interface Reconstruction. *J. Comput. Phys.* 93, 449–468.
- Austin, D.I., Schlueter, R.S., 1982. A numerical model of wave breaking/breakwater interactions. In: *Proceedings 18th International Conference on Coastal Engineering*, Vol. 3. Cape Town, Republic of South Africa, pp. 2079–2096.
- Brorsen, M., Larsen, J., 1987. Source generation of nonlinear gravity waves with boundary integral equation method. *Coastal Eng.* 11, 93–113.
- Chopra, A., Greated, C.A., 1995. Development and validation of the Volume of Fluid technique for water wave dynamics. In: *Proceedings of the 6th International symposium on Computational Fluid Dynamics*, NV, USA, pp. 212–217.
- Christensen, M., 1995. Generation and active absorption of 2- and 3-dimensional water waves in physical models. PhD thesis, Aalborg University, Aalborg, Denmark. ISSN 0909–4296.
- Frigaard, P., Brorsen, M., 1995. A time-domain method for separating incident and reflected irregular waves. *Coastal Eng.* 24, 205–215.
- Frigaard, P., Christensen, M., 1994. An absorbing wave-maker based on digital filters. In: *Proceedings, 24th International Conference on Coastal Engineering*, Vol. 1. Kobe, Japan, pp. 168–180.
- Hald, T., Frigaard, P., 1996. Performance of active wave absorption systems — comparison of wave gauge and velocity meter based systems. In: *Proceedings 2nd International Conference on Coastal, Ports and Marine Structures*. ICOPMAS, Tehran, Iran.
- Hirt, C.W., Nichols, B.D., 1981. *J. Comput. Phys.* 39, 201–225.
- Iwata, K., Kawasaki, K., Kim, D., 1996. Breaking limit, breaking and post-breaking wave deformation due to submerged structures. In: *Proceedings 25th International Conference on Coastal Engineering*, Vol. 3. Orlando, USA, pp. 2338–2351.
- Kothe, D.B., Mjolsness, R.C., Torrey, M.D., 1991. RIPPLE: a computer program for incompressible flow with free surfaces. Report LA-12007-MS, Los Alamos Scientific Report, Los Alamos, NM, USA.
- Kothe, D.B., Ferrell, R.C., Turner, J.A., Mosso, S.J., 1997. A high resolution finite volume method for efficient parallel simulation of casting processes on unstructured meshes. Los Alamos National Laboratory Report LA-UR-97-30. In: *Proceedings 8th SIAM Conference on Parallel Processing for Scientific Community*. Minneapolis, MN, USA.
- Larsen, J., Dancy, H., 1983. Open boundaries in short wave simulations — a new approach. *Coastal Eng.* 7, 285–297.
- Lemos, C.M., 1992. Wave breaking, a numerical study. *Lecture Notes in Engineering* No. 71. Springer-Verlag, Berlin, Germany.
- Nichols, B.D., Hirt, C.W., Hotchkiss, R.S., 1980. SOLA-VOF: a solution algorithm for transient fluid flow with multiple free boundaries. Report LA-8355, Los Alamos, CA, USA.
- Petit, H.A.H., van den Bosch, P., 1992. SKYLLA: wave motion in and on coastal structures. Numerical analysis of program modifications. Delft Hydraulics Report H1351. Delft, The Netherlands.
- Sabeur, Z.A., Allsop, N.W.H., Beale, R.G., Dennis, J.M., 1996. Wave dynamics at coastal structures: development of a numerical model for free surface flow. In: *Proceedings 25th International Conference on Coastal Engineering*, Vol. 1. Orlando, USA, pp. 389–402.
- Schäffer, H.A., Klopman, G., 1997. Review of multidirectional active wave absorption methods. In: *Proceedings of the I.A.H.R. seminar on multidirectional waves and their interaction with structures*, 27th I.A.H.R. Congress. San Francisco, USA, pp. 159–182.
- Sethian, J.A., 1997. Tracking interfaces with level sets. *American Scientist* 85 (3), 254–263.
- Shyy, W., 1994. Computational modeling for fluid flow and interfacial transport. *Transport processes in engineering*, Vol. 5. Elsevier.
- Torrey, M.D., Cloutman, L.D., Mjolsness, R.C., Hirt, C.W., 1985. NASA-VOF2D: a computer program for incompressible flows with free surfaces. Report LA-10612-MS. Los Alamos Scientific Report, Los Alamos, NM, USA.
- Troch, P., 1997. VOFbreak², a numerical model for simulation of wave interaction with rubble mound breakwaters. In: *Proceedings 27th IAHR Congress*. San Francisco, USA, pp. 1366–1371.
- Troch, P., De Rouck, J., 1998. Development of 2D numerical wave flume for simulation of wave interaction

- with rubble mound breakwaters. In: Proceedings 26th International Conference on Coastal Engineering. Copenhagen, Denmark.
- Van der Meer, J.W., Petit, H.A.H., van den Bosch, P., Klopman, G., Broekens, R.D., 1992. Numerical simulation of wave motion on and in coastal structures. In: Proceedings 23rd International Conference on Coastal Engineering, Vol. 2. Venice, Italy, pp. 1772–1784.
- Van Gent, M.R.A., 1995. Wave interaction with permeable coastal structures. PhD thesis Technical University Delft. Delft, The Netherlands. ISBN 90-407-1182-8.
- Van Gent, M.R.A., Tönjes, P., Petit, H.A.H., van den Bosch, P., 1994. Wave action on and in permeable coastal structures. In: Proceedings 24th International Conference on Coastal Engineering, Vol. 2. Kobe, Japan, pp. 1739–1753.
- Waller, M.N.H., Christakis N., Allsop N.W.H., Beale R.G., Dennis J.M., 1998. Development and validation of a numerical model of wave dynamics. In: Proceedings 17th International Conference on Offshore Mechanics and Arctic Engineering. Lisbon, Portugal.
- Welch, J.E., Harlow, F.H., Shannon, J.P., Daly, B.J., 1966. The MAC method: a computing technique for solving viscous incompressible, transient fluid flow problems involving free surface. Report LA-3425, Los Alamos Scientific Report, Los Alamos, CA, USA.
- Wu, N., 1994. Numerischen simulation der druckschlagbelastung durch brechende wellen auf senkrechte bauwerke. PhD thesis Französisches Institut für Wasserbau und Küsteningenieurwesen - Universität Hannover, Hannover, Germany.